AIAA JOURNAL
Vol. 49, No. 5, May 2011

Microvortex Generators Applied to Flowfield Containing a Normal Shock Wave and Diffuser

Neil Titchener* and Holger Babinsky†
University of Cambridge, Cambridge, England CB2 1PZ, United Kingdom

DOI: 10.2514/1.J050760

The flow through a terminating shock wave and the subsequent subsonic diffuser typically found in supersonic inlets has been simulated using a small-scale wind tunnel. Experiments have been conducted at an inflow Mach number of 1.4 using a dual-channel working section to produce a steady near-normal shock wave. The setup was designed so that the location of the shock wave could be varied relative to the diffuser. As the near-normal shock wave was moved downstream and into the diffuser, an increasingly distorted, three-dimensional, and separated flow was observed. Compared with the interaction of a normal shock wave in a constant area duct, the addition of the diffuser resulted in more prominent corner interactions. Microvortex generators were added to determine their potential for removing flow separation. Although these devices were found to reduce the extent of separation, they significantly increased three-dimensionality and even led to a large degree of flow asymmetry in some configurations.

Nomenclature

C_f	=	$\tau_w/\frac{1}{2}\rho_{fs}u_{fs}^2$, local skin friction coefficient
D	=	$(p_{02,\max} - p_{02,\min})/\bar{p}_{02}$, flow distortion
h	=	microvortex generator height
H_i	=	incompressible boundary-layer shape factor (δ_i^*/θ_i)
p_i	=	time-averaged wall pressure at station i
$\bar{p}_0$	=	area-averaged pressure recovery at the pitot rake ($\bar{p}_{02}/p_{01}$)
p_{0i}	=	time-averaged stagnation pressure at station i
u	=	time-averaged streamwise velocity
u^*	=	$\sqrt{\tau_w/\rho_w}$, wall-shear velocity
u_{fs}	=	time-averaged freestream streamwise velocity
w	=	tunnel half-width, 57 mm
x	=	streamwise displacement relative to diffuser entrance
x_{VG}	=	position of microvortex generator trailing edge
y	=	wall-normal displacement
z	=	spanwise displacement from tunnel centerline
z'	=	z/w
δ	=	boundary-layer thickness based on $0.99u_{fs}$
Δx	=	distance between baseline separation and microvortex generator trailing edge
δ_i^*	=	incompressible boundary-layer displacement thickness
θ_i	=	incompressible boundary-layer momentum thickness
ρ	=	time-averaged density
ρ_{fs}	=	time-averaged freestream density
ρ_w	=	time-averaged wall density
τ_w	=	time-averaged wall-shear stress

Subscripts

0	=	station 0, nozzle exit ($x = 67$ mm)
1	=	station 1, upstream of normal shock wave
2	=	station 2, at pitot rake location

Presented as Paper 2010-0590 at the 48th AIAA Aerospace Sciences Meeting and Exhibit, Orlando, FL, 4–7 January 2010; received 9 July 2010; revision received 9 December 2010; accepted for publication 3 January 2011.

*Research Student, Fluid Mechanics, Department of Engineering, Trumpington Street. Student Member AIAA.

†Professor in Aerodynamics, Department of Engineering, Trumpington Street. Associate Fellow AIAA.

I. Introduction

WITH the exception of the scramjet, all current airbreathing engine technology requires subsonic flow for combustion. This poses a particular problem in supersonic applications because of the requirement to decelerate the flow significantly before the engine. This is usually achieved using a system of oblique shock waves, which are an efficient means of compression, followed by a terminal shock wave within the inlet. Unfortunately, the interaction of these shock waves with the inlet boundary layers [shock wave/boundary-layer interactions (SWBLIs)] results in boundary-layer thickening and can trigger separation, both of which lead to large losses and distortion at the engine face.

To avoid flow distortion and to maximize inlet pressure recovery, wall suction or bleed is frequently employed to improve boundary-layer performance by removing low momentum fluid from the near-wall region via a number of holes, slots, or scoops. Although effective, conventional bleed systems result in reduced mass flow to the engine, thereby reducing engine thrust. To compensate, the engine inlet has to be larger, increasing weight and drag. Such a system also leads to a more complex inlet design, again increasing both weight and drag.

Recently, there has been a resurgence in interest in the use of vortex generators (VGs) to reduce separation in engine inlets [1–5]. These passive devices induce streamwise vortices that transfer high momentum fluid from the freestream to the boundary layer while simultaneously removing low momentum fluid from the near-wall region. Of specific interest are devices often referred to as microvortex generators (μVGs) or sub-boundary-layer VGs. These VGs, generally defined as those with heights less than a boundary-layer thickness, have been found to offer a similar level of mixing but with a reduced drag penalty when compared with larger devices [6,7]. The main advantage of VGs over wall suction is their simple and passive design, which results in no decrease in mass flow to the engine. Their ability to be used alongside conventional bleed systems is also advantageous. However, before they can be introduced into the design of supersonic inlets, our understanding of these devices must be improved.

Until now, most studies of μVGs in SWBLIs have been performed in simple flowfields, such as the flat-plate normal or oblique SWBLI [1–4]. The flow in a real inlet, however, is considerably more complex. In particular, the boundary layer is subjected to multiple shock wave interactions and, after the terminating shock wave, it also encounters a subsonic diffuser that imposes an additional adverse-pressure gradient. Previous investigations on single shock wave interactions alone (whether normal shock or oblique shock) do not provide information on the extent to which SWBLI flow control can alter the ability of the boundary layer to deal with the subsequent

diffuser, or whether flow control capable of beneficially affecting a SWBLI can also improve the coupled shock/diffuser problem. The study reported here therefore combines the effects of a terminating shock wave and a subsonic diffuser in order to address this problem; thus, it addresses at least some of the additional complexity found in a realistic diffuser flow.

II. Experimental Arrangement

All experiments were undertaken in the blowdown-type supersonic wind tunnels at the University of Cambridge. The setup within the working section is shown in Fig. 1. The interaction of interest occurs below the shock holder, and it is primarily contained within the area viewable through the tunnel windows. The incoming Mach number and the subsonic diffuser ramp angle were selected to approximate typical inlet flow conditions and, on the basis of a review of the available literature, Mach 1.4 and 6° were chosen as appropriate values. Typically, inlets with such parameters require extensive flow control to perform satisfactorily, and it is thought that this is, therefore, a suitable starting point for an assessment of the potential of novel control techniques. The use of a shock holder allows the position of the terminating shock wave to be controlled more easily. The shock holder improves shock stability as it allows spillage over the upper side of the holding plate [8]. In this configuration, the working section is split into two channels: a lower choked section and an upper unchoked and supersonic section. Such a configuration eliminates the problem of large-scale unsteadiness (or even unstart) that has been known to occur in similar uncontrolled flowfields [7].

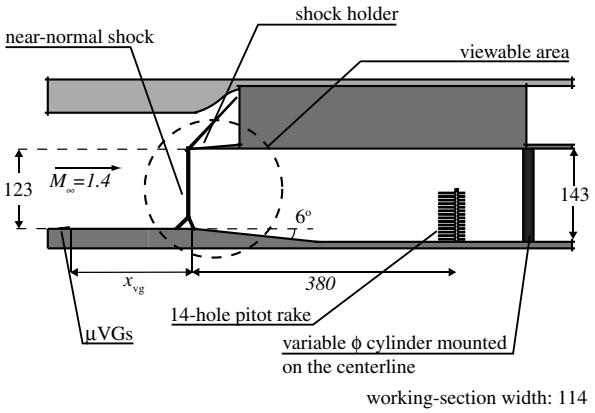

a) Wind-tunnel schematic

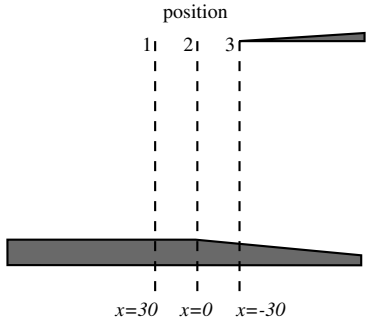

b) Shock holder positions relative to the diffuser entrance

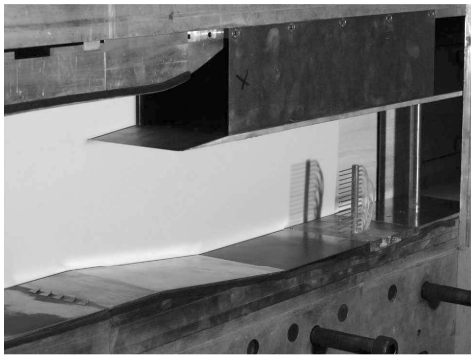

c) Photograph of experimental arrangement

Fig. 1 Wind-tunnel setup (all dimensions in mm).

For all experiments, the stagnation temperature of the tunnel was within the range 290 ± 5 K and the stagnation pressure was nominally set to 205 kPa. This results in a nominal Reynolds number of 26×10^6 m^{-1}, and the variations in stagnation temperature and pressure result in a maximum variation in Reynolds number of less than 5%. At such high Reynolds numbers, these variations can be assumed to have a negligible effect on the flow.

Flow visualization has been carried out using a two-mirror schlieren system, and the surface flow has been visualized using a mixture of paraffin, titanium dioxide, and oleic acid. Schlieren images were taken with a digital single-lens reflex camera at shutter speeds of 1/800 s. Surface and pitot pressures were measured using pressure transducers mounted outside the tunnel. Wall-pressure distributions were also measured using a pressure-sensitive paint (PSP) system consisting of an ultraviolet light source and an acrylic-based paint containing a luminescent dye. The luminescent dye emits red light at an intensity related to its partial pressure, allowing the wall-pressure distribution to be calculated. The error in the PSP system is thought to be ±5%. A rake of 14 pitot probes was used to determine the stagnation pressure distribution downstream of the diffuser at the simulated engine face or aerodynamic interface plane (AIP) (see Fig. 1). The pitot rake spanned the vertical range $5 \leq y \leq 70$ mm with a (constant) 5 mm resolution. The rake could be positioned at seven spanwise locations, $-48 \leq z \leq 48$, with a 16 mm resolution, allowing three-dimensional contour plots of the downstream flow to be produced. The experimental error in the pressure transducers for the surface and pitot pressure measurements is of the order of 1%. The absolute spatial accuracy of each pitot probe is thought to be around 0.5 mm. However, the difference in wall-normal placement of the rake between runs is negligible, allowing comparisons to be made with confidence. The incoming flow was measured using laser Doppler anemometry (LDA), and the accuracy of the LDA system is in the range ± 1 ms^{-1}.

The setup was designed so that the position of the shock holder could be adjusted easily and, as such, three different shock positions were examined. The three positions are shown in Fig. 1: position 1 ($x = 30$), position 2 ($x = 0$), and position 3 ($x = -30$). The position of the terminating shock wave was controlled by varying the downstream area near the exit of the lower section, and the mass flow was regulated in this way using different diameter wall-normal cylinders positioned on the centerline. Cylinders were required with diameters between 15 and 18 mm, and these cylinders were placed a minimum of eight cylinder diameters downstream of the AIP, so as to not significantly influence measurements at this plane.

The near-normal shock wave was located close to the lip of the shock holder by observing the schlieren image of the tunnel and adjusting the blockage accordingly. This typically led to an average shock wave standoff in the range 1–2 mm, giving a small amount of spillage over the top of the shock holder. By keeping the position of the terminating shock near constant throughout this investigation, the VG ability to improve the flowfield through momentum transfer, and not through a modification to the shock position, can be ascertained.

III. Characterization of Incoming Boundary Layer

The incoming boundary-layer properties were measured using LDA. These data are shown in Fig. 2, where the measured inflow boundary-layer profile is plotted alongside the generic turbulent boundary-layer fit proposed by Sun and Childs [9]. This plot, along with the wall-coordinate plot shown in Fig. 2b, displays excellent agreement between the analytically derived profile and that obtained from measurements, demonstrating that the inflow boundary layer closely resembles a fully developed zero-pressure-gradient turbulent boundary layer.

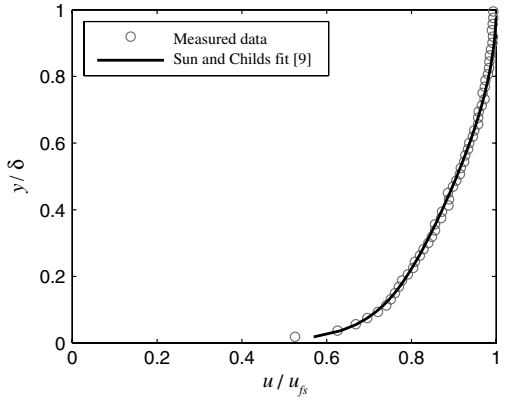

a) Mean velocity profile

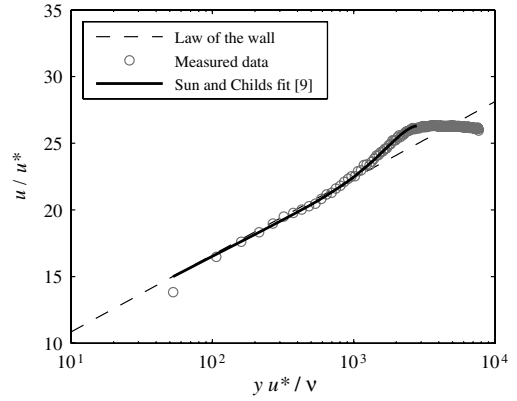

b) Mean velocity profile in log-law coordinates

Fig. 2 Mach 1.4 incoming boundary-layer properties; LDA measurements and Sun and Childs fits shown [9].

Both the boundary-layer thickness and the value of the skin-friction coefficient were derived from this analytical fit. Their values, among other boundary-layer parameters, are also shown in Fig. 2. The Reynolds number based on incoming incompressible displacement thickness δ^*_{i0} was found to be 14,000. The LDA-derived velocity data also allow the boundary-layer characteristics and the appropriate scaling for the VGs with incoming boundary-layer thickness δ_0 to be determined.

Assuming that the sidewall boundary layers are approximately the same thickness as the tunnel-floor boundary layer, a confinement parameter (here defined as the ratio of boundary-layer area to tunnel working-section area) was estimated to be around 2.5%.

IV. Uncontrolled Interactions

First, results are presented for the three baseline cases. Schlieren images for the three shock positions investigated are shown in Fig. 3. Figure 3a shows a schlieren image of the working-section setup with the shock holder in position 1 ($x = 30$ mm). The black area around the image indicates the edge of the schlieren mirror. The interaction regions for positions 1, 2, and 3 are shown in enlarged form in Figs. 3b–3d. The faint oblique Mach wave that can be seen in the bottom left-hand corner of the schlieren images is from the join between the diffuser and nozzle block. Its effect is negligible.

With the shock holder in position 1 ($x = 30$ mm), the schlieren images (Figs. 3a and 3b) illustrate a number of the features typical of a transonic SWBLI, and these features have been labeled for clarity in Fig. 3a. The shock is bifurcated in the near-wall region, with the front leg emanating from the position where the boundary layer starts to thicken, and this front leg reaches the inviscid part of the shock at the triple point. The thickening of the boundary layer continues through the interaction, with the boundary layer only flattening off once it passes the rear leg of the shock, behind which there are a number of weak shocklets. This region of near-sonic flow is often referred to as the supersonic tongue, and it indicates reacceleration of the near-wall flow because of the boundary-layer thickening. Once the boundary layer enters the diffuser, it is difficult to tell whether this layer remains attached or detaches, and as such, the viscous region from this point downstream is referred to as a shear layer. The main body of the shock wave stands close to vertical just in front of the lip of the shock holder; however, the slight shock curvature indicates that the shock is, in fact, a strong oblique solution of the Rankine–Hugoniot equations rather than a truly normal shock solution. This is a consequence of the nonuniform flow downstream of the shock wave as a result of boundary-layer thickening and separation on the floor, and flow spillage ahead of the splitter plate.

When the shock wave is moved downstream to position 2 ($x = 0$), the shock structure looks similar, with a small increase in boundary-layer thickening across the interaction when compared with position 1. A much larger change in shock structure is observed when the shock holder is moved downstream to position 3 (see Fig. 3d). In this figure, there is a notable increase in the boundary-layer thickening across the interaction, which is also indicated by the movement of the triple point away from the wall. The main body of the shock is also more highly curved, especially in the region above the triple point. The boundary layer also continues to thicken behind the rear leg of the shock wave, unlike before, and as such, at the edge of the image, the shear layer/boundary layer is thicker than in positions 1 and 2. Although the shock holder is inside the diffuser, the strength of the shock wave appears to not have increased, as any expansion around the corner of the diffuser entrance is swallowed by the shock foot.

Oil flow visualizations, shown in Fig. 4, reveal substantial changes to the near-wall flow as the shock is moved downstream toward the diffuser. In position 1, the oil flow indicates that there is no large-scale separation along the tunnel centerline: neither beneath the shock nor in the diffuser. Nevertheless, there is an area of low shear stress beneath the shock, indicated by a whiter footprint in this region. The lack of shock-induced separation along the tunnel centerline is in agreement with experiments conducted in this tunnel of a flat-plate transonic SWBLI [10]. As well as this, corner separations are visible, originating at the shock-foot location. These corner separations remain relatively small, like the flat-plate case, until the start of the diffuser where they start to expand again. The flow is also closely symmetric. This lack of shock-induced separation at this relatively high Mach number is discussed in detail by Burton et al. [11] and is thought to be a result of three-dimensional effects. Agreement between the surface-flow visualizations obtained in position 1 and in a configuration without a diffuser is evidence that the diffuser is too far downstream to have any significant detrimental effect in the interaction region itself.

In position 2, there is a marked change in the flowfield. Most visible in Fig. 4b is the large change to the corner separations. It is evident that these sidewall interactions are strongly affected by the shock position closer to the diffuser: large sidewall separations originate at the shock foot. These structures grow quickly with streamwise distance and, at their widest point, cover more than half of the tunnel span. The flow in these corner separations seems to circulate around a central point. Again, there appears to be no shock-induced separation along the tunnel centerline. Downstream of the shock foot, there is a large region of reversed flow in the diffuser indicated by the almost two-dimensional separation line produced between the two corner interactions. The position of the separation line well downstream of the shock foot suggests that the adverse-pressure gradient of the diffuser is required on top of that of the shock wave to cause detachment. The oil flow picture is also relatively symmetric, with only a slight skew of the centerline observed.

When the shock wave is pushed further downstream, the sidewall interactions are again very prominent, almost filling the whole tunnel span. These corner interactions also have clear foci, indicating that they wrap up into vortices in this instance. The main difference to position 2 is that the centerline flow now separates in the shock-foot location, which has been indicated in Fig. 4. The flow is also very

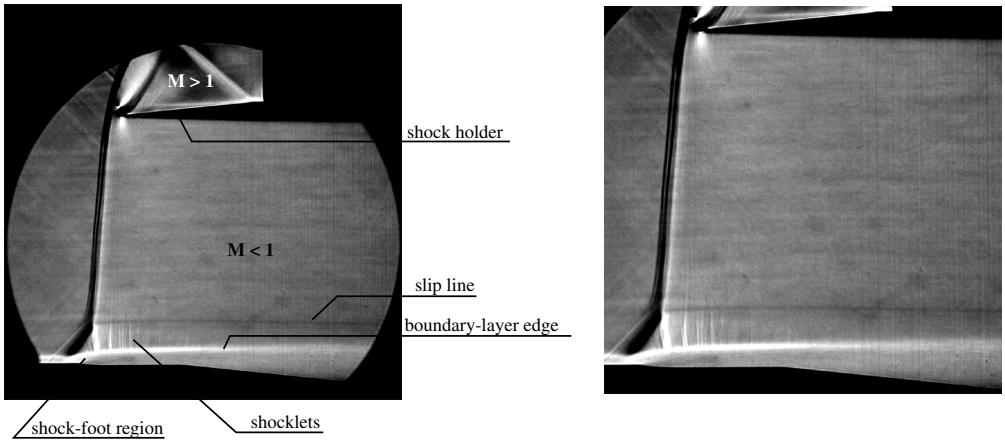

a) Position 1; overview

b) Position 1

c) Position 2

d) Position 3

Fig. 3 Schlieren overviews (left) and close-ups (right) for each of the baseline interactions.

symmetric. The reattachment line for the centerline flow is downstream of the diffuser and at a similar location for both positions 2 and 3.

Wall-pressure profiles of the centerline flow, measured using both pressure transducers and PSP, are shown in Fig. 5. It can be seen that there is generally good agreement between the PSP data and the pressure transducers. There is a small discrepancy at some streamwise locations when the shock holder is in position 1, and it is unclear as to why this is. In Fig. 5b, each of these profiles and a flat-plate Mach 1.4 wall-pressure profile have been superimposed on top of one another so that the initial pressure rise starts at the same location. It can be seen that all the curves collapse to a single line in the first portion of the interaction. This agreement continues until the profile for position 3 starts to plateau, which occurs just at the start of the diffuser. This leveling off of the pressure rise, and the plateau thereafter, are synonymous of separation. Downstream of the diffuser entrance, the pressure profiles for all three positions start to deviate significantly in response to the different distances between the shock wave and diffuser.

It is apparent that, in position 3, the flow is overcome by separation, and there is only a very slow increase in pressure in the diffuser, with the initial pressure in the diffuser lower than in the flat-plate case. This reduced pressure rise is likely to be due to separation observed in this case, which is not present in the flat-plate case. The plateauing of the pressure rise just inside the diffuser occurs at a pressure of approximately 0.49, which agrees well with the pressure level at separation predicted by the free interaction concept [12,13]. By moving the shock upstream to position 2, it can be seen that the flow is able to diffuse significantly more than in position 3, although the rise does flatten off in the diffuser as a result of the separation shown in the surface-flow visualization. Moving the shock further upstream to position 1 results in further static pressure recovery than before. In position 1, the inflexion point at the entrance to the diffuser suggests that the pressure rises from the SWBLI and diffuser have not fully merged (this inflexion is more easily observed by looking at the pressure transducer measurements). This response of the wall-pressure distribution to the diffuser entrance also indicates that the flow is attached here. When comparing the profile for position 1 with the flat-plate interaction profile, it can be seen that even upstream of the diffuser entrance the pressure is higher in position 1 than in the flat-plate case. The diffuser is undoubtedly influencing the flow upstream of its entrance. Again, in position 1, the pressure rise flattens off in the second half of the diffuser, evidence that the thickening of the shear layer at this point is approaching the rate of increasing area. There appears to be a clear advantage to placing the transonic SWBLI further upstream from the diffuser entrance: with each movement forward, there is a linear improvement in normalized recovery of approximately 0.05.

These findings are is general agreement with the oil flow visualizations and schlieren images. The centerline wall-pressure profile for position 3 verifies that there is no expansion fan around the diffuser entrance: the wall-pressure profile already rising before this point.

The total pressure measured at the AIP for each of the shock positions is shown in Fig. 6. The lines bounding these plots on the left and right indicate the tunnel sidewalls. Clear from these figures is a thickening of the shear layer on the tunnel floor as the shock is moved downstream: this thickening shear layer resulting in the lower diffusion observed in the wall-pressure profiles. At the same time as this, the loss of total pressure also increases in the near-wall region, indicated by the darker regions close to the wall. This is more clearly shown in Fig. 7, which shows the increase in losses along the tunnel centerline as the shock is moved closer to the diffuser. The increase in pressure recovery in the outer region for position 3 is thought to be a result of the shock's strong oblique behavior, which results in lower entropy creation across the shock wave.

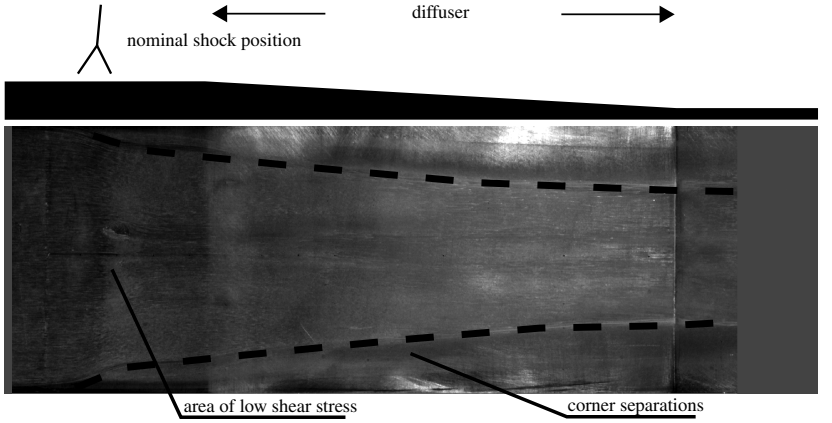

a) Position 1

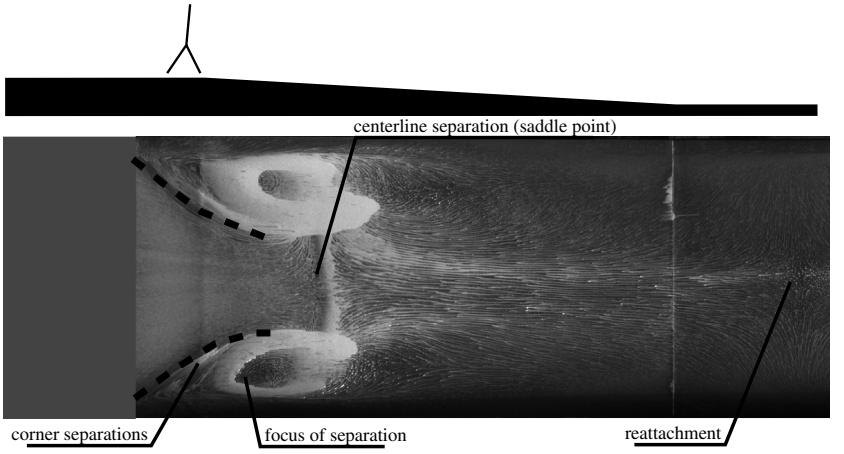

b) Position 2

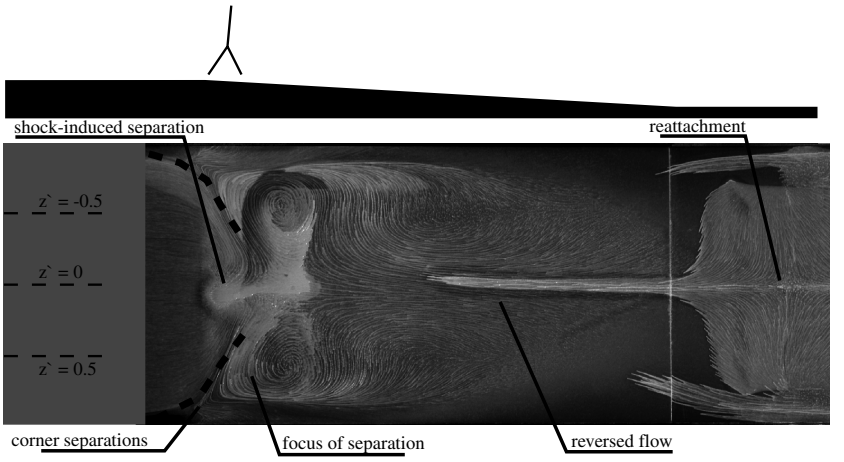

c) Position 3

Fig. 4 Oil flow for the three uncontrolled cases with shock in positions 1, 2, and 3, respectively.

From Fig. 6, a notable change to the variation of losses across the tunnel span is also observed: the flow changes from having concave isobars in the near-wall region in position 1 to having convex curvature in position 3. The convex curvature in position 3 is thought to be caused by streamwise vortices, and these may be the same vortices that initiate from the foci of the corner interactions in Fig. 4c. These streamwise vortices transfer higher total pressure flow from the outer flow toward the wall (see Fig. 6c). Also indicated in these figures is the area-averaged total pressure and distortion, defined here as the maximum difference in total pressure, nondimensionalized by the area-averaged total pressure. The average total pressure drops almost linearly at around 2.5% between shock positions, with the distortion rising slowly.

Between positions 1, 2, and 3, little difference in the stagnation pressure profiles was measured when the rake was placed closest to the sidewalls. Although the sidewall boundary layers may be of similar extent at this location, the low resolution in this region makes it difficult to make conclusive observations about their extent and health (the pitot rake only penetrates to approximately 50% of the sidewall boundary-layer thickness). The only indication of differences in sidewall behavior is seen through the spanwise variation of the tunnel-floor flow.

These measurements show that there is a clear disadvantage to placing the shock too close to the diffuser. By placing the shock wave right in the vicinity of the diffuser, the boundary layer immediately downstream of the shock has little, if any, time to recover before

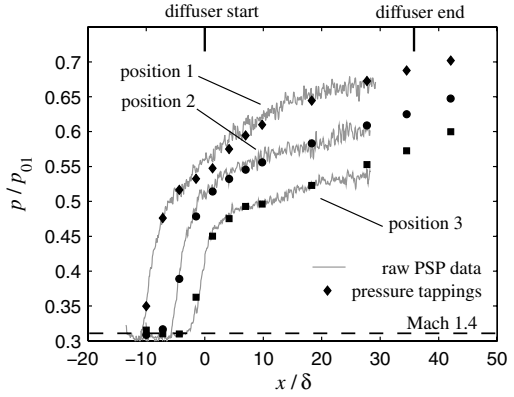

a) Baseline wall pressures profiles

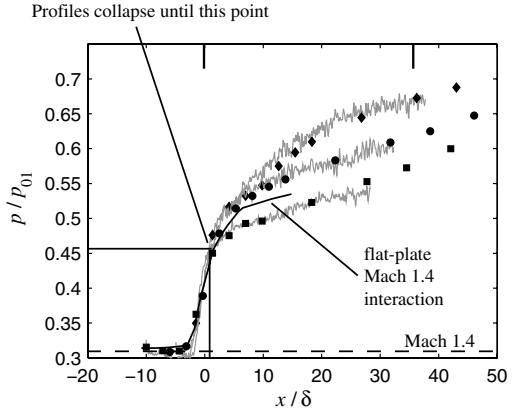

b) Baseline wall pressures with offset profiles

Fig. 5 Variation of wall pressure throughout interaction and diffuser for the baseline cases.

being subjected to a second adverse pressure gradient. From the data, it is evident that the flow is highly sensitive to shock positioning close to the diffuser entrance. Only if the shock-induced pressure gradient and the diffuser pressure gradient are separated by a sufficient distance, allowing the boundary layers time to recover, are relatively benign corner interactions observed. It is thought that by continuing to move the shock wave upstream, an optimal location may be found, after which no further improvements to the downstream flow can be made. However, in these experiments, such a location was not found. It is still unclear how the precise geometry in the vicinity of the shock effects the interaction, and more work is required to obtain a better understanding of this flow. The difference in the flowfields obtained in positions 1 and 2 indicates that the floor boundary layer requires approximately 2δ downstream of the shock foot to recover before it can be subjected to another adverse-pressure gradient without separating.

The significance of the sidewall interactions in each of the uncontrolled cases has resulted in a flowfield that differs somewhat from that which would be found in a typical inlet. In general, two-dimensional external compression-type inlets are unlikely to have such substantial boundary layers on three sides, as is the case in these experiments and, as such, the corners would not be as dominant. Nevertheless, the corner interactions observed here would occur in these similar flowfields, but their relative importance depends on the aspect ratio and size (relative to the boundary-layer thickness) of the inlet duct.

V. Vortex Generator Designs

Two types of μVGs were examined. The microramp that has, up until now, been the most extensively used μVG in the literature [1–5], and a new type of μVG, the robust vane (r vane), designed in house. The geometries of the two μVG configurations are shown in Fig. 8. The new type of VG tested here, the r vane, is expected to

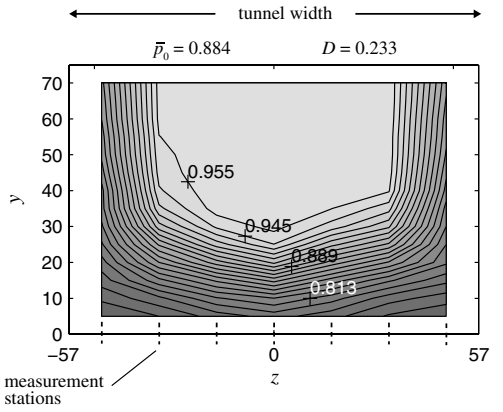

a) Position 1

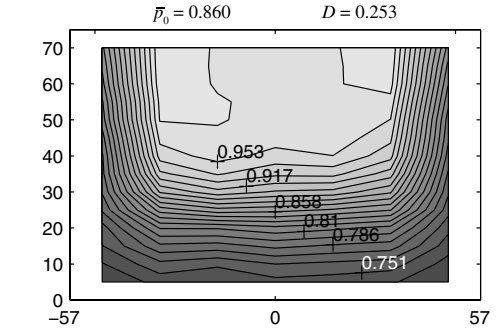

b) Position 2

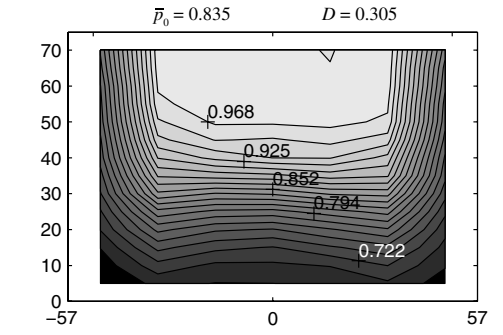

c) Position 3

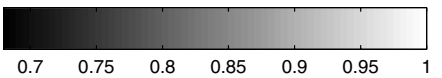

Fig. 6 Total pressure profiles for the baseline cases, looking downstream. The dashed lines on the abcissa for position 1 indicate measurement locations.

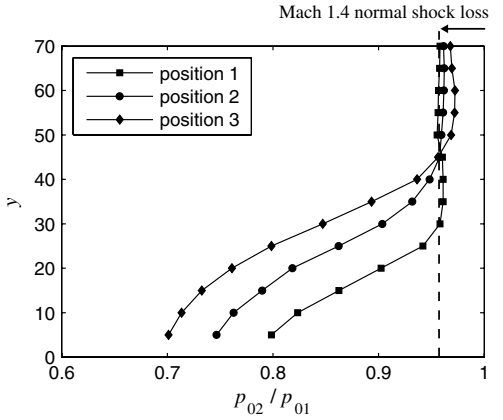

Fig. 7 Centerline total pressure profiles for shock in positions 1, 2, and 3.

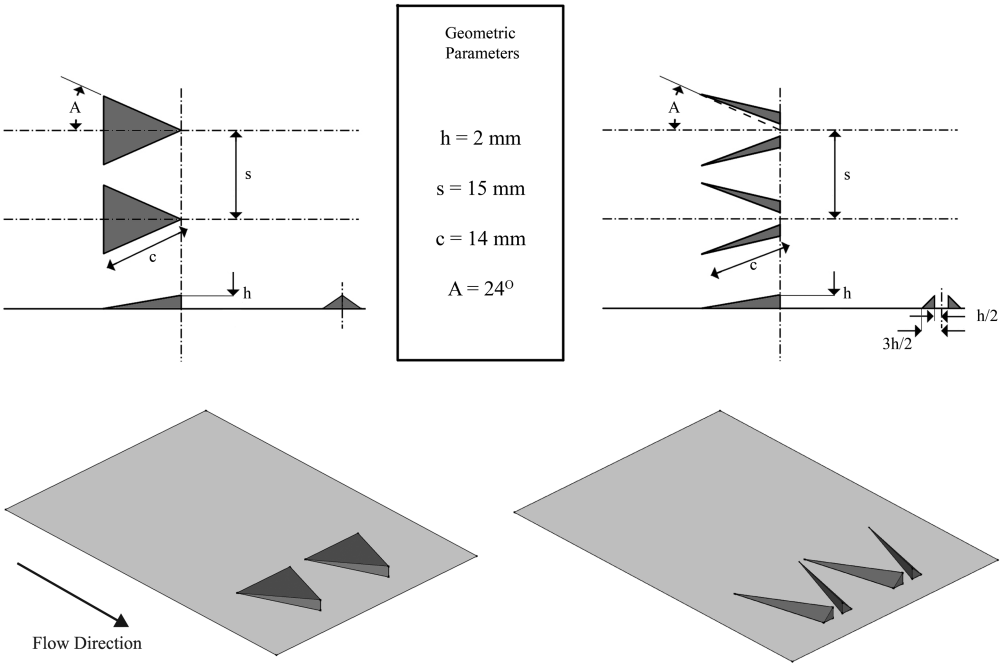

a) Microramp **b) *r* vanes**

Fig. 8 VG geometries.

provide a good compromise between vorticity generation and physical robustness. Compared with a standard vane-type VG, there is significantly more contact area for fixation to the inlet walls and lower susceptibility to bending or accidental damage, much like the microramp. Yet, a recent experimental investigation has suggested that the *r* vane may produce enhanced levels of mixing when compared with the microramp [14].

The baseline flow has revealed extensive separation along the floor and in the corners. Ideally, flow control would address both of these problem areas; however, previous research has shown that the placement of μVGs ahead of corner flow regions has been detrimental, i.e., leading to large increases in corner separation [15]. On the other hand, μVGs have shown potential for controlling separations observed away from corners, such as seen here on the floor of the working section in positions 2 and 3. Therefore, μVGs were positioned so that they did not interact with the incoming sidewall boundary-layer flows. Consequently, arrays were limited to five μVGs. The μVGs were added upstream of the shock, and all arrays were placed symmetrically across the tunnel.

Microramps and *r* vanes were placed upstream of the shock, with the shock holder in position 3. The nondimensional height of both types of μVG with respect to the incoming boundary-layer thickness is $h/\delta_0 = 0.38$. The microramps were tested at four positions upstream of the diffuser entrance: $x_{VG} = 3, 33, 63$, and 93 mm. These values correspond to a distance upstream of the baseline separation normalized by device height ($\Delta x/h$) of 5, 20, 35, and 50.

VI. Controlled Interactions

A schlieren image of the interaction region with microramps is shown in Fig. 9. The μVGs are visible in the bottom left-hand corner. The two oblique shocks radiating from the microramps are the result of boundary-layer thickening in the vicinity of the μVG leading and trailing edges. This leads to a thicker boundary layer approaching the interaction when compared with the baseline case. Although the oblique shocks from the μVGs are visible in the schlieren images far downstream (intersecting with the normal shock), by this time, they are merely Mach waves and have virtually no effect on the near-normal shock. Compared with Fig. 3, there is a less pronounced lambda shock structure and no distinct triple point. The viscous region downstream of the shock is also more blurred than before.

Surface oil flow visualizations with the microramps are shown in Fig. 10. From these pictures, it is clear that the devices are not able to eliminate separation; however, in each case, a thin attached channel is achieved between the large recirculating separations on either side. These corner flows, again, originate near the nominal shock location and are elongated when compared with before. At the same time, the reattachment line downstream of the diffuser has moved upstream when compared with the baseline case. These surface visualizations also suggest that the flow is relatively insensitive to μVG positioning; nevertheless, an optimum upstream distance at which the extent of the centerline separation is minimized was found to be $\Delta x/h = 35$.

To make a direct comparison with microramps, *r* vanes were tested at the optimal streamwise location for the microramps. Some surface oil flow visualizations obtained with pairs of *r* vanes are shown in Fig. 11. A set of five pairs of *r* vanes, which is directly comparable with the microramps, is shown at the top of Fig. 11. The resulting surface-flow visualization exhibits very different features from that obtained with the microramps. The most prominent feature is the highly asymmetric flowfield, with one corner interaction occupying around 75% of the tunnel span. At the same time, coupled with this, there is no separation along the central streamtube that, although highly skewed by the presence of the corner interactions, remains

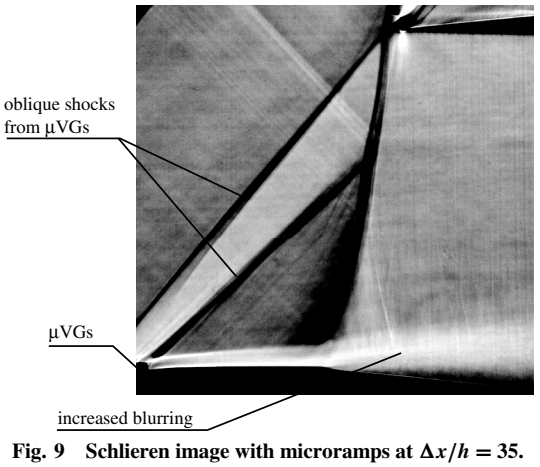

Fig. 9 Schlieren image with microramps at $\Delta x/h = 35$.

attached throughout the domain. This test case was repeated to eliminate the possibility that an air leak or an error in μVG placement was the cause of such asymmetry. The outcome of these tests was a near-perfect reproduction of this flowfield. The *r* vanes appear to influence the near-wall flow very significantly, and this is our first indication that *r* vanes produce stronger vortices than the microramps. When comparing the vortex footprints of the microramps and *r* vanes from the surface oil flow visualizations, it is difficult to obtain any conclusive evidence of the relative vortex strengths due to the small size of these devices.

A number of different *r* vane arrays were tested to explore this phenomenon further, and surface-flow visualizations for these are shown in Figs. 11b–11d. It is clear that, as the number of pairs of *r* vanes are reduced, centerline separation returns and flow symmetry are gradually restored. These findings suggest that the use of stronger flow control (i.e., more pairs of *r* vanes) can lead to asymmetrical solutions. With only two pairs of *r* vanes, the flowfield looks relatively similar to that with the five-microramps case, and there is a similar extent of attached flow between the two corner interactions (see Fig. 11d). In this configuration, the vortices from the *r* vanes appear to be quickly swept toward the tunnel centerline, and this may therefore be why an attached channel between the two corners is produced in this case. As well as the asymmetry, it can be seen that in no configuration can a significant spanwise extent of attached flow be obtained. Also, in all cases, the corner vortices are again enlarged by the presence of flow control on the tunnel floor. The importance of the corner flows is compounded by the inability to obtain a symmetrical flow in many of the configurations.

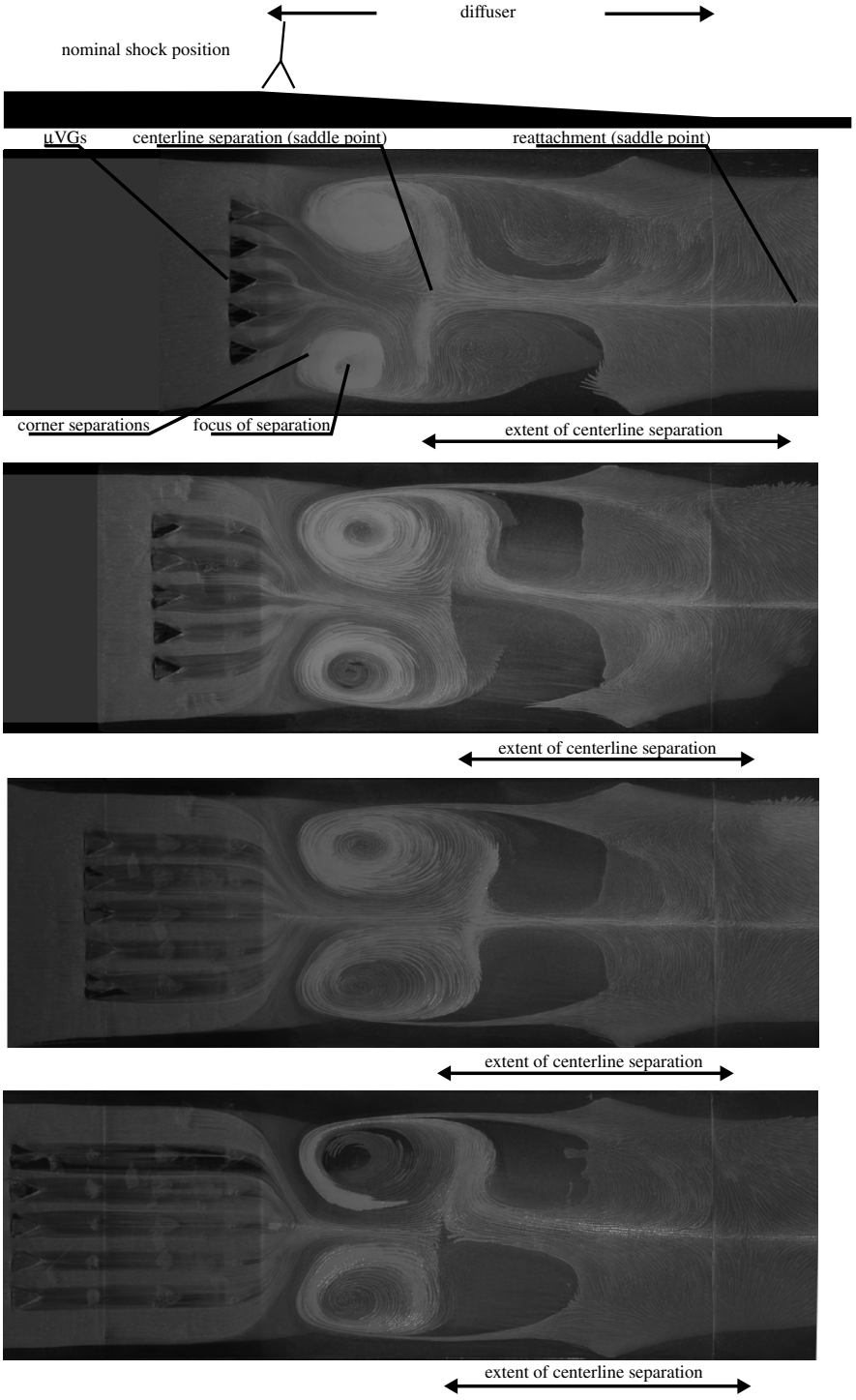

Fig. 10 Microramps placed at $\Delta x/h$ equal to 5, 20, 35, and 50, respectively.

These surface-flow visualizations suggest that trying to energize the tunnel floor leads to larger corner interactions and, in some cases, with substantial energization near the centerline, asymmetrical solutions can be obtained.

In Fig. 12a, the wall-pressure distributions with five microramps and five pairs of r vanes at $\Delta x/h = 35$ are compared with the baseline case. One sees a small increase in the overall pressure rise with the addition of μVGs. However, all three profiles follow each other closely over the first half of the diffuser. In contrast, the behavior of the offcenterline wall-pressure distributions vary somewhat between the three cases in the interaction region, as can be seen in Fig. 12b (the spanwise locations of these offcenterline distributions are shown in Fig. 4c). These smoothed PSP measurements show a clear increase in the upstream influence distance away from the centerline in the baseline case, after which both offcenterline profiles follow the centerline profile relatively closely. With the addition of the microramps, the offcenterline pressure profiles plateau at a pressure significantly below the centerline profile. This is probably due to the corner separations; nevertheless, by halfway down the diffuser, the offcenterline profiles rejoins the centerline profile. In agreement with the surface-flow visualizations, a symmetrical flow is indicated by the minimal discrepancy between the two offcenterline profiles for both the baseline case and the case with microramps. With the inclusion of the five pairs of r vanes, the offcenterline wall-pressure distributions look somewhat different from the baseline and microramp cases. Immediately obvious is the

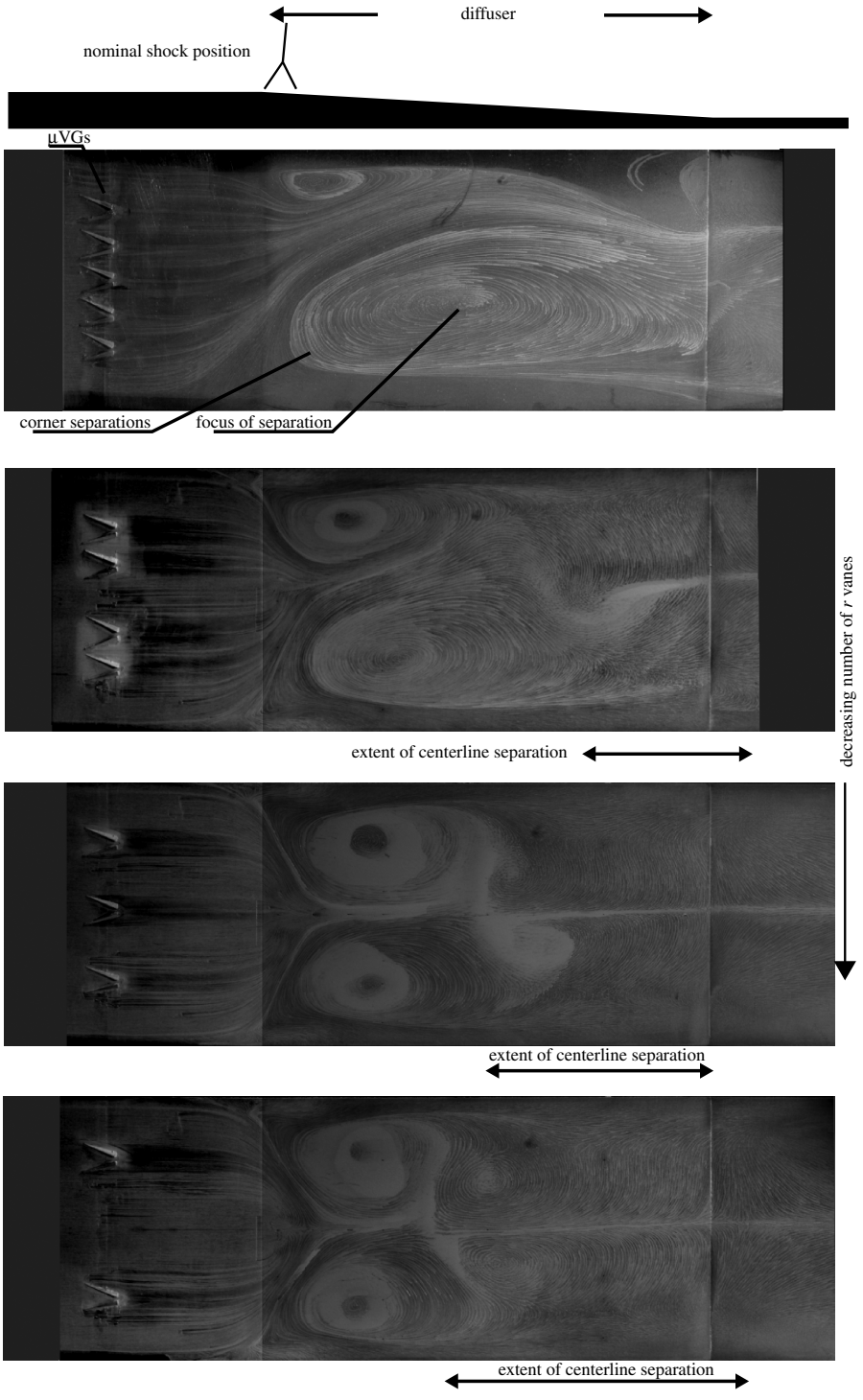

Fig. 11 Arrays of five, four, three, and two pairs of *r* vanes.

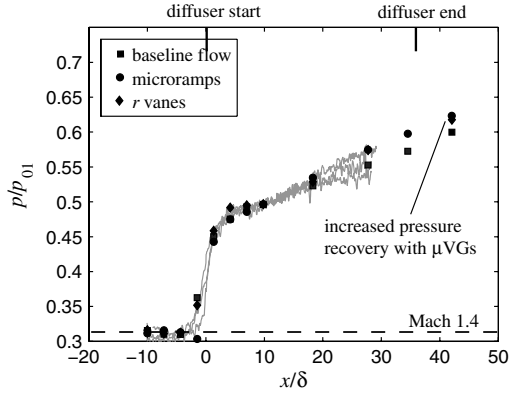

a) Centerline wall-pressure profiles for the baseline flow, microramps, and *r* vanes in position 3

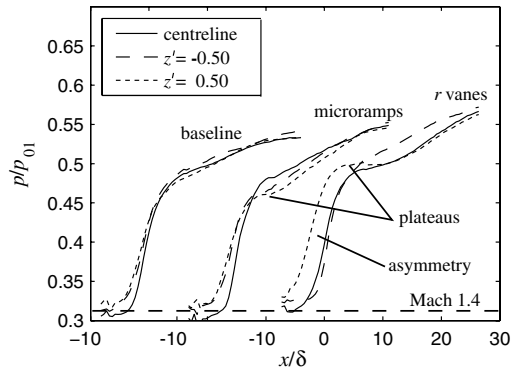

b) Spanwise variation of wall-pressure profiles for the baseline flow, microramps, and *r* vanes

Fig. 12 Wall-pressure variation with and without μVGs.

asymmetry, which is in good agreement with the surface-flow visualization. Both the $z' = 0.50$ and the centerline profile exhibit a prominent plateau, which is a result of the very large corner covering both one side and the centerline flow. Whereas, the flow at $z' = -0.50$ rises continually, as this location is close to the location where the attached streamtube passes.

One explanation for the increase in corner separations observed with flow control is that reduced separation along the center of the tunnel increases the effective area change along the diffuser, which in turn imposes a greater pressure gradient elsewhere. Since no flow control was employed along the sidewalls and in the corners, this results in increased separation there, counteracting the beneficial effects seen along the floor. As a result, overall, there is little static pressure recovery change from the baseline case. Nevertheless, the central streamtube gains somewhat from a delayed separation, and the sidewall interactions lose out, with higher stagnation pressure loss in these regions. A similar conflict between the centerline flow and sidewall flows has been observed by Burton et al. [11] as well as by Bruce et al. [16]. If the corners become so large that they are able to interact, then this interaction may lead to the large-scale asymmetry [17]. Similar asymmetry to that observed in these experiments was obtained by Morris et al. [18] with the use of boundary-layer control in the form of suction on the tunnel-floor flow. In this case, the sidewalls were also left uncontrolled.

The total pressure profile at the AIP obtained with the five microramps and the five pairs of *r* vanes are shown in Fig. 13. From these distributions, it is clear that the μVGs have managed to reduce the stagnation pressure losses in the near-wall region. In the case of the microramps, the region of loss is of a similar thickness to before, but the extent of the losses are partially reduced in the near-wall region. The average pressure recovery is increased by 1.5%, and the distortion rises from 0.305 to 0.336. The flow also appears reasonably symmetrical. The total pressure profile at the AIP with the inclusion of *r* vanes is shown in Fig. 13b. It can be seen that there is an improvement in the near-wall region at the location where the attached streamtube that passes between the sidewall interactions meets the rake. As expected, there is significant asymmetry, and the large losses in the positive z side are apparent. Because of the detrimental effect the *r* vanes have had on the sidewalls, the average pressure recovery remains practically unchanged (0.846 compared with 0.844) compared with the microramps, and the distortion is further increased. The *r* vane effect on the flowfield is emphasized in Fig. 13c, in which the change in total pressure between the baseline case and the case with the *r* vanes is shown. Immediately clear is the improvement on the side where the central streamtube is swept, and the high losses associated with the large corner interaction are also visible.

These results emphasize that, to determine the potential benefits of different μVG configurations in more two-dimensional conditions typically found in engine inlets, the corner interactions must first be controlled. At the same time, our fundamental understanding of these corner flows should also be improved due to their presence in a variety of applications. It is thought that the overall total pressure recovery can only be substantially improved if the corner flows and centerline flow are both controlled.

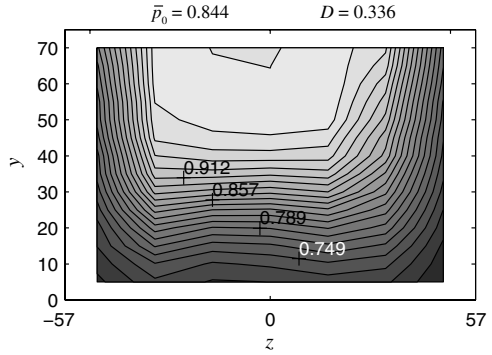

a) Microramps

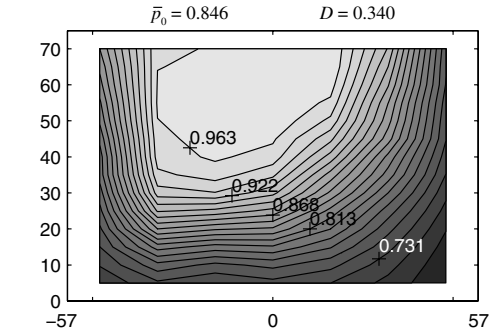

b) *r* vanes

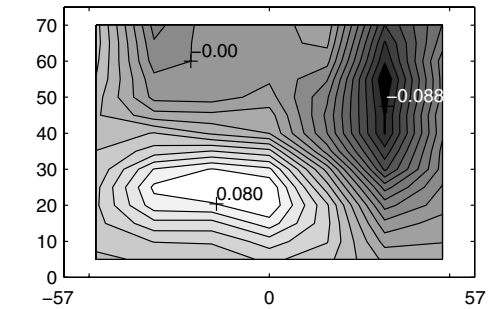

c) Net effect of *r* vanes

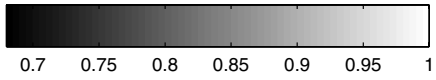

Fig. 13 Total pressure profiles (note that the color bar is not valid for Fig. 13c).

VII. Conclusions

The flow through a terminating near-normal shock wave and a subsequent diffuser have been investigated. The conclusions of this study are as follows:

1) When the near-normal shock wave is placed far enough upstream of the diffuser, attached flow is achieved along the centerline, throughout the interaction and in the diffuser, and there are relatively small corner separations. As the shock wave is moved closer to the diffuser, separation appears along the tunnel centerline. Once a separated region exists, further downstream movement of the shock moves the centerline separation point forward to beneath the shock foot, even though no increase in the upstream Mach number is observed. As the shock wave is moved downstream, lower pressure recovery (both total and static) is observed and distortion is increased. It is clear that the diffuser has a strong influence on the flow when placed in the close vicinity of the SWBLI.

2) As well as inducing centerline separation, moving the shock wave downstream also significantly increases the size of the corner separations, with a highly three-dimensional flowfield observed in position 3. Moreover, the influence of the corner flows is somewhat exaggerated by the relatively narrow tunnel working section and, in a real inlet, these flows would be less prominent. Nevertheless, corner flows are an important phenomenon that are, as yet, not fully understood.

3) Microramps and *r* vanes were able to partially remove separation from the centerline, and this resulted in higher total pressure recovery in the near-wall region at the AIP. At the same time as suppressing centerline separation, both microramps and *r* vanes tended to enlarge and elongate the corner structures. As a result, the increase in both average total pressure and static pressure was confined to a limited area away from corner effects and, overall, integral improvements were small. This enlargement of the corner interactions is thought to be caused by the tunnel centerline flow trying to induce a stronger pressure rise in the diffuser.

4) In some configurations, the application of flow control causes the flow to become asymmetrical, although the reasons for this are not yet known. A possible interaction between the two corners may be the cause of asymmetry.

5) The beneficial effects of flow control are, to a great extent, eradicated by a significant increase in the size and severity of corner separations. This highlights that any application of flow control in an inlet-relevant flowfield must address both the sidewall/floor boundary-layer interactions and the corner flow problem. To date, no flow control device (other than bleed) has proven capable of minimizing corner effects, and future research is needed to identify nonbleed control methods. The physics observed here suggest that different approaches are needed for the corner flow problem and the quasi-two-dimensional flow separation, typically observed in more fundamental studies.

Acknowledgments

This effort is sponsored by the U.S. Air Force Office of Scientific Research, U.S. Air Force Material Command, under grant number FA8655-08-1-3091. The views and conclusions contained herein are those of the authors and should not be interpreted as necessarily representing the official policies or endorsements, either expressed or implied, of the U.S. Air Force Office of Scientific Research or the U.S. Government. The authors would like to thank P. Bruce for his support throughout this project.

References

[1] Babinsky, H., Li, Y., and Ford, C. W. P., "Microramp Control of Supersonic Oblique Shock Wave/Boundary-Layer Interactions," *AIAA Journal*, Vol. 47, No. 3, March 2009, pp. 668–675. doi:10.2514/1.38022

[2] Lee, S., Goettke, M., Loth, E., Tinapple, J., and Benek, J., "Microramps Upstream of an Oblique-Shock/Boundary-Layer Interaction," *AIAA Journal*, Vol. 48, No. 1, Jan. 2010, pp. 104–118. doi:10.2514/1.41776

[3] Ghosh, S., Choi, J., and Edwards, J., "Numerical Simulations of Effects of Micro Vortex Generators Using Immersed-Boundary Methods," *AIAA Journal*, Vol. 48, No. 1, Jan. 2010, pp. 92–103. doi:10.2514/1.40049

[4] Anderson, B. H., Tinapple, J., and Surber, L., "Optimal Control of Shock Wave Turbulent Boundary Layer Interactions Using Micro-Array Actuation," 3rd AIAA Flow Control Conference, AIAA Paper 2006-3197, June 2006.

[5] Titchener, N., and Babinsky, H., "Micro-Vortex Generators Applied to a Flowfield Containing a Normal Shock Wave and Diffuser," 48th AIAA Aerospace Sciences Meeting and Exhibit, AIAA Paper 2010-0590, 2010.

[6] Rao, D., and Kariya, T., "Boundary-Layer Submerged Vortex-Generators for Turbulent Flow Separation Control: An Exploratory Study," AIAA/ASME/SIAM/APS 1st National Fluid Dynamics Congress, Cincinnati, OH, AIAA Paper 1988-3546, July 1988.

[7] Babinsky, H., Morgan, C., and Makinson, N., "Micro-Vortex Generator Flow Control for Supersonic Engine Inlets," 45th AIAA Aerospace Sciences Meeting and Exhibit, Reno, NV, AIAA Paper 2007-0521, Jan. 2007.

[8] Babinsky, H., and Ogawa, H., "Wind-Tunnel Setup for Investigation of Normal Shock Wave/Boundary-Layer Interaction Control," *AIAA Journal*, Vol. 44, No. 11, Nov. 2006, pp. 2803–2805. doi:10.2514/1.24370

[9] Sun, C., and Childs, M., "A Modified Wall Wake Velocity Prole for Turbulent Compressible Boundary Layers," *Journal of Aircraft*, Vol. 10, No. 6, 1973, pp. 381–383. doi:10.2514/3.44376

[10] Bruce, P., and Babinsky, H., "An Experimental Study of Transonic Shock/Boundary Layer Interactions Subject to Downstream Pressure Perturbations," *Aerospace Science and Technology*, Vol. 14, No. 2, 2010, pp. 134–142. doi:10.1016/j.ast.2009.11.006

[11] Burton, D., Bruce, P., and Babinsky, H., "Experimental Investigation into the Parameters Governing Corner Interactions for Transonic Shock Wave/Boundary-Layer Interactions," 48th AIAA Aerospace Sciences Meeting and Exhibit, Orlando, FL, AIAA Paper 2010-0871, Jan. 2010.

[12] Chapman, D. R., Kuehn, D. M., and Larson, H. K., "Investigation of Separated Flow in Supersonic and Subsonic Streams With Emphasis on the Effect Of Transition," NACA, TN 3869, Washington, D.C., 1957.

[13] Erdos, J., and Pallone, A., "Shock/Boundary-Layer Interaction and Flow Separation," *Proceedings of the Heat Transfer and Fluid Mechanics Institute Proceedings*, Stanford Univ. Press, Stanford, CA, 1962.

[14] Li, Y., "Supersonic Inlets," Internal Report, Cambridge Univ., Cambridge, U.K., June 2008.

[15] Bruce, P., "Transonic Shock/Boundary Layer Interactions Subject to Downstream Perturbations," Ph.D. Thesis, Univ. of Cambridge, Cambridge, U.K., 2008.

[16] Bruce, P., Burton, D., Titchener, N., and Babinsky, H., "Corner Flows and Separation in Transonic Channel Flows," *45th Symposium of Applied Aerodynamics*, 3AF, Marseille, March 2010.

[17] Bruce, P., Babinsky, H., Tartinville, B., and Hirsch, C., "Corner Effects and Asymmetry in Transonic Channel Flows," *AIAA Journal* (submitted for publication).

[18] Morris, M. J., Sajben, M., and Kroutil, J. C., "Experimental Investigation of Normal-Shock/Turbulent-Boundary-Layer Interactions with and Without Mass Removal," *AIAA Journal*, Vol. 30, No. 2, Feb. 1992, pp. 359–366. doi:10.2514/3.10926

L. Cattafesta
Associate Editor